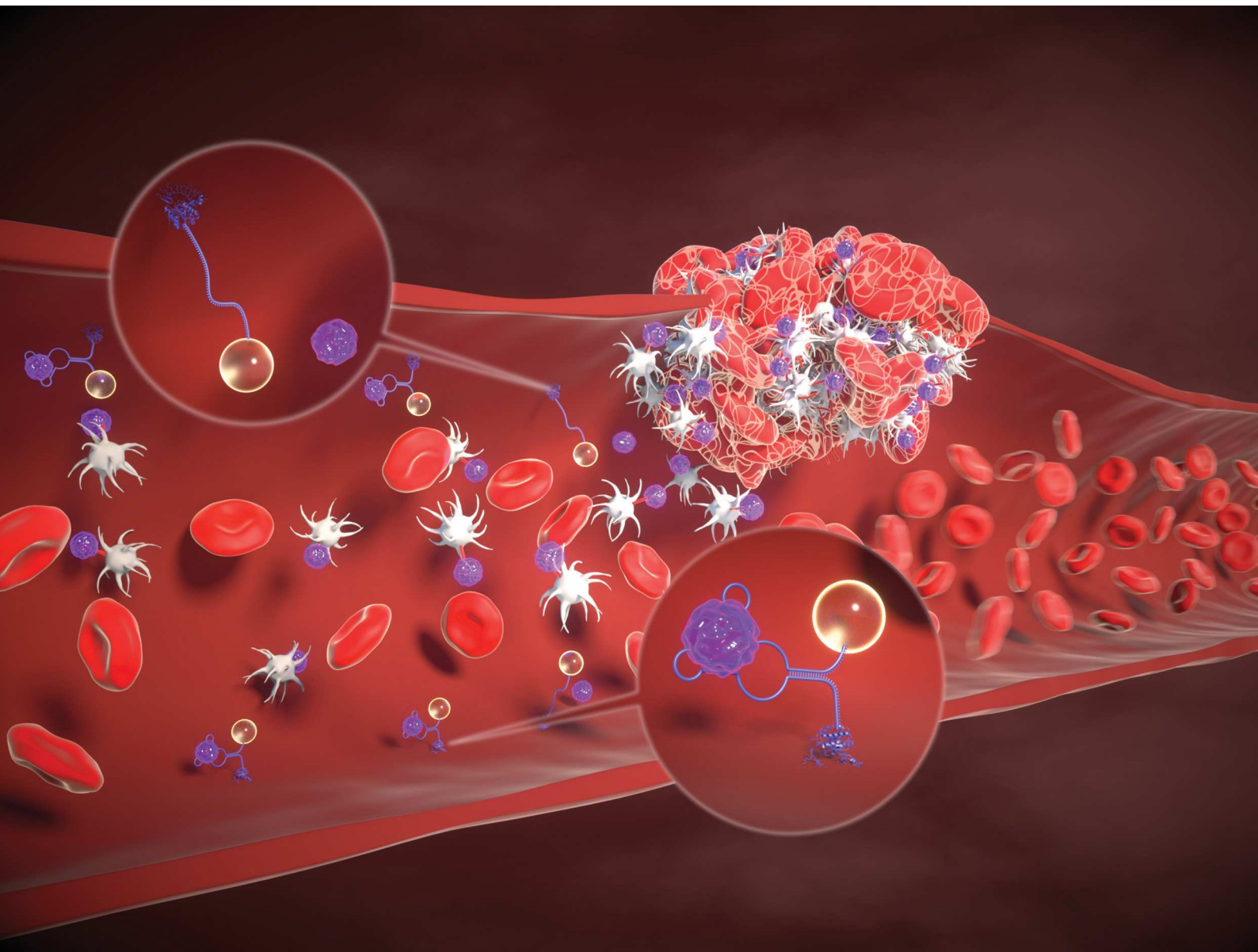
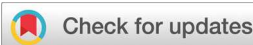


Nanoscale

rsc.li/nanoscale



ISSN 2040-3372



Cite this: *Nanoscale*, 2025, **17**, 1246

Aptamer-based biotherapeutic conjugate for shear responsive release of Von Willebrand factor A1 domain[†]

Esraa Ismail, ^a Yi Liu, ^{a,c} Yi Wang, ^{b,d} Sajedehalsadat Yazdanparast Tafti, ^a X. Frank Zhang^c and Xuanhong Cheng ^{*a,b}

Smart polymers that mimic and even surpass the functionality of natural responsive materials have been actively researched. This study explores the design and characterization of a Single-MOlecle-based material REsponsive to Shear (SMORES) for the targeted release of A1, the platelet binding domain of the blood clotting protein von Willebrand factor (VWF). Each SMORES construct employs an aptamer molecule as the flow transducer and a microparticle to sense and amplify the hydrodynamic force. Within the construct, the aptamer, ARC1172, undergoes conformational changes beyond a shear stress threshold, mimicking the shear-responsive behavior of VWF. This conformational alteration modulates the bioavailability of its target, the VWF-A1 domain, ultimately releasing it at elevated shear. Through optical tweezer-based single-molecule force measurement, ARC1172s role as a force transducer was assessed by examining its unfolding under constant pulling force. We also investigated its refolding rate as a function of force under varied relaxation periods. These analyses revealed a narrow range of threshold forces (3–7 pN) governing the transition between folded and unfolded states. We subsequently constructed the SMORES material by conjugating ARC1172 and a microbead, and immobilizing the other end of the aptamer on a substrate. Single-molecule flow experiments on immobilized SMORES constructs revealed a peak A1 domain release within a flow rate range of (40–70 $\mu\text{L min}^{-1}$). A COMSOL Multiphysics model translated these flow rates to total forces of 3.10 pN–5.63 pN experienced by the aptamers, aligning with single-molecule force microscopy predictions. Evaluation under variable flow conditions showed a peak binding of A1 to the platelet glycoprotein Ib (GPIB) within the same force range, confirming released payload functionality. Building on knowledge of aptamer biomechanics, this study presents a new strategy to create shear-stimulated biomaterials based on single biomolecules.

Received 1st July 2024,
Accepted 9th October 2024

DOI: 10.1039/d4nr02715a
rsc.li/nanoscale

1. Introduction

Designing stimulation-responsive materials has been an area of active research for the past few decades. These smart materials allow us to emulate the adaptability observed in living systems, offering the potential for advanced functional-

ities surpassing those found in nature. Among the wide range of physical simulations, shear stress plays a crucial role in numerous physiological functions.^{1–4} In particular, shear stress in the circulatory system contributes significantly to various normal and pathological processes. Designing drug delivery vehicles possessing shear-switchable activities represents a novel approach to rectifying malfunction of the circulatory system.

Shear-dependent bulk properties have long been studied and explored for biomedical applications.^{5–7} For example, hydrogels made of synthetic polymers, polysaccharides, and polypeptides have been shown to liquefy into an injectable state at high shear, and they have been studied as drug delivery carriers and tissue engineering scaffolds.^{8–11} DNA-based supramolecular hydrogels with a viscoelastic behavior that is sensitive to temperature, ion concentration, and shear have been adapted for tissue engineering and 3D bioprinting.¹² Additionally, extensive research has been conducted to under-

^aDepartment of Bioengineering, P. C. Rossin College of Engineering and Applied Science, Lehigh University, Bethlehem, Pennsylvania, USA

^bDepartment of Materials Science and Engineering, P. C. Rossin College of Engineering and Applied Science, Lehigh University, Bethlehem, Pennsylvania, USA.
E-mail: xuc207@lehigh.edu

^cDepartment of Biomedical Engineering, University of Massachusetts Amherst, Amherst, MA, USA

^dCurrent Address: Analytical Research and Development, Merck & Co., Inc. Greater Philadelphia, Pennsylvania, USA

[†]Electronic supplementary information (ESI) available: Gel electrophoresis results, aptamer-A1 binding affinity by optical tweezers, and COMSOL multiphysics modelling. See DOI: <https://doi.org/10.1039/d4nr02715a>

stand the impact of shear flow on the behavior of molecular assemblies at the micro and nanoscale. For example, liquid crystals have been demonstrated to change photoluminescence triggered by shear-induced phase transition.^{13,14} Shear deformable nanoparticles such as spherical liposomes, lenticular liposomes, inorganic nanospheres, nanogels, and micellar hydrogels have been extensively studied for targeted drug delivery applications. Nanoparticle and microparticle aggregates have been shown to disperse under high shear flow conditions within blood vessels, facilitating payload delivery and enabling controlled release.^{15,16}

In contrast to the extensive research conducted on polymer solution rheology and molecular/particle assemblies, attempts in engineering single-molecule flow responders are very limited. In the former case, shear responses are primarily determined by intermolecular interactions, whereas the conformation of single molecules relies heavily on intramolecular secondary forces. Thus, the flow responses of bulk polymers and molecular/particle assemblies *versus* single molecules involve different physical processes. In addition, molecular/particle ensembles with a large enough collective dimension experience significant shear stress in the physiological range.¹⁷ On the other hand, most polymeric molecules are too small to have a significant conformational change in the physiologically relevant shear rate range. Nonetheless, single molecules with ultra-high molecular weights¹⁸ on the order of a million Daltons or larger could be shear-responsive, as exemplified by the blood coagulation factor, von Willebrand factor (VWF).

VWF is a large multimeric protein composed of normally tens, but sometimes up to hundreds of monomers, each with a molecular weight of 280 kDa. Synthesized by endothelial cells, sub-endothelial connective tissues, and megakaryocytes, VWF plays a pivotal role in both hemostasis and thrombosis.¹⁹ VWF assumes a globular shape and is essentially inert under typical blood flow conditions, but its functionality is activated on multiple length scales in response to sufficient hydrodynamic stresses. Unraveling, on a macromolecular level, reveals previously hidden active sites that are otherwise deeply buried within the globule.^{20–22} Further changes on a submonomer level activate functionalities such as the A1 domain, which binds to the platelet receptor GPIB and promote coagulation at the site of bleeding. This activation involves internal tension of the A1 domain and force-dependent structural changes in the A2 domain that inhibits the A1 domain function at the resting state.^{20,23–26} The interaction between VWF and platelets is crucial for maintaining hemostasis within healthy parameters. In addition, the A1 domain alone^{27,28} has been shown to initiate platelet activation and aggregation without the need of the full VWF molecule. Inspired by the unique structure and function of VWF, in this research study, we carried out a rational design of a Single-MOLEcule based material with structures and functions REsponsive to Shear (SMORES), built on the understanding of how flow modulates the physical and biochemical behaviors of single VWF molecules. Despite its great structural complexities, VWF can be conceptualized into three basic building blocks: the ultra-large, multimeric struc-

ture serves as a flow sensor; the flexible A2 domain and A1–A2 linker serve as the force transducer that convert a mechanical force into a conformational change; and the A1 domain is the function executor that captures platelets after being unblocked. To mimic the function of VWF, the SMORES material uses a microparticle to sense and amplify the hydrodynamic force, with aptamer molecules serving as the flow transducer/switch. The drag force experienced by the particle is transduced to the aptamer molecule and alters its conformation, modulating the structure of the aptamer and the bioavailability of its target, the VWF-A1 domain, thereby achieving single-molecule flow activation similar to VWF (Fig. 1).

Aptamers have previously been utilized as biosensors²⁹ and drug delivery vehicles³⁰ for the triggered release of anticancer drugs.³¹ In the realm of cardiovascular diseases, aptamers have been developed into therapeutics such as antithrombotic and anti-coagulation agents by targeting coagulation factors as well as endothelial and mesenchymal stem cell membrane receptors.^{32,33} Aptamers inhibiting VWF-induced platelet activation and thrombosis have been reported,^{34–36} including the natural DNA aptamer ARC1172 (KD = 326 pM),³⁷ which binds to and blocks the function of the VWF A1 domain. ARC1172 has been studied as an antiplatelet agent in hemostasis therapy, leveraging its antithrombotic activity by targeting the A1 domain of activated VWF.³⁷ While aptamers are popular affinity agents, this study is the first to explore how mechanical force regulates the binding affinity of a selected aptamer towards its ligand. Specifically, ARC1172 was investigated as a force transducer in a construct that releases the A1 domain at sites of pathological shear to initiate clotting. The aptamer-based shear-sensitive construct mimics the shear-regulated function of VWF, and holds potential for managing bleeding conditions such as Von Willebrand Disease (VWD).³⁸

2. Experimental

2.1 Mechanical properties of aptamer ARC1172 by single molecular force microscopy

The DNA sequence used in this work consists of 75 bases with the following sequence: 5'- /5ThioMC6-D/TTT TTT TTT TTT TTT TTT TTT TTT TTT TGG CGT GCA GTG CCT TCG GCC GTG CGG TGC CTC CGT CAC GCC TTT TTT TTT/3Bio/-3' (IDT, Coralville, IA). The underlined segment represents the reported sequence of aptamer ARC1172,³⁹ while the flanking portions of the sequence consisting of thymine bases extended the aptamer from the surface during immobilization. The sequence contains a biotin group at the 3' end and a thiol modifier C6 S–S (disulfide) at the 5' end for further modification.

To investigate the mechanical properties of the aptamer-based sequence as a molecular force transducer, its unfolding extension was first characterized under different constant loading rates and pulling forces using single-molecule force measurements by optical tweezers. In this setup, the aptamer bridges two microbeads to form a singular tether (Fig. 2A). The

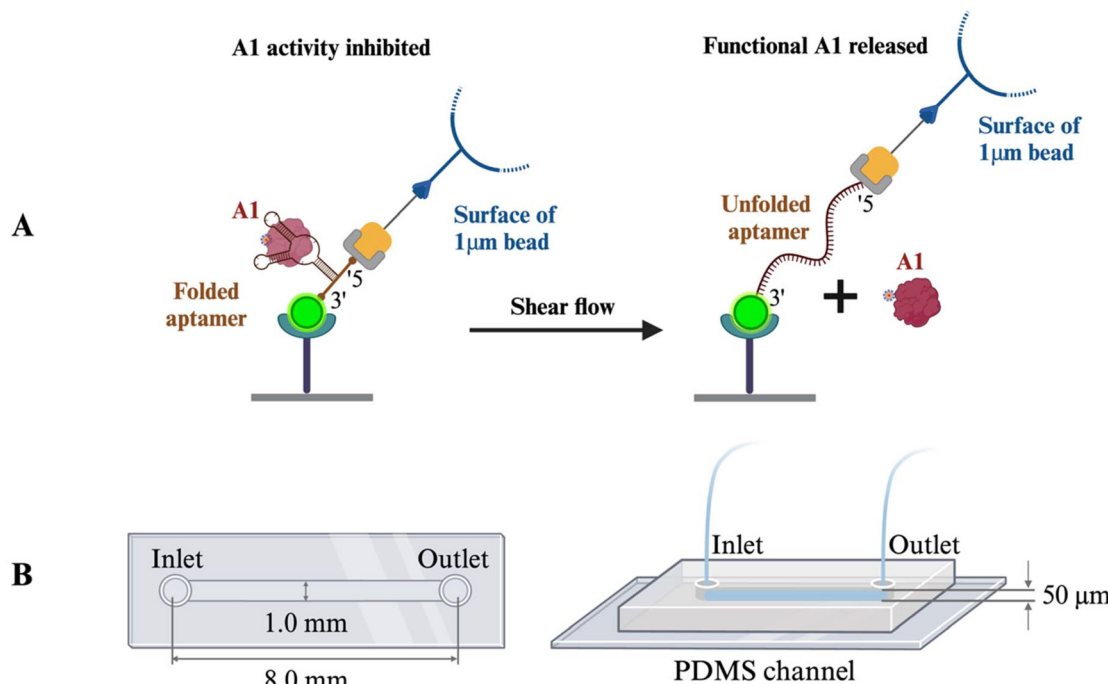


Fig. 1 Schematics summarizing the immobilization and flow modulation of the structure and function of the SMORES construct. (A) Schematics of flow test for the aptamer-based shear-responsive flow sensor. The SMORES construct was immobilized onto the microfluidic surface through the biotin-streptavidin interaction. Quantum dot-or biotin-labelled A1 domains were used to quantify the release of the payload from the aptamer under variable flow conditions (B) Dimensions of the PDMS microfluidic channel used for flow experiments.

bead-aptamer-bead sandwich structure was constructed through the following steps.

First, the aptamer was conjugated to SpyTag (GenScript Biotech, Piscataway, NJ) on the 5' end. The thiol group of the aptamer was reduced with 1,4-dithiothreitol (DTT, Sigma-Aldrich, St Louis, MO) at room temperature for 1 hour at a 1 : 10 molar ratio of aptamer to DTT. Simultaneously, ethylenediaminetetraacetic acid (EDTA, Thermo Fisher Scientific, Waltham, MA) was mixed with the aptamer at a 1 : 10 molar ratio of aptamer to EDTA. EDTA was added to the reduction reaction to chelate divalent metals, thereby preventing disulfide formation in the sulphydryl-containing aptamer. DTT and EDTA were then removed with Micro Bio-Spin chromatography columns (Bio-Rad laboratories, Hercules, CA), and the buffer was exchanged with 0.2 M sodium acetate buffer (pH = 5).

After the reduction step, the thiol group of the aptamer was activated by reaction with 2,2'-dithio-dipyridine (DTDP, Sigma-Aldrich) for 2 hours at room temperature at a 1 : 5 molar ratio of aptamer to DTDP. The aptamer was then purified from DTDP using a Pierce Concentrator (Thermo Fisher Scientific). In parallel, the thiol group on the cysteine of SpyTag was reduced by DTT at room temperature for 1 hour. Excess DTT was then filtered from the SpyTag solution using a Slide-A-Lyzer MINI dialysis device (Thermo Fisher Scientific) through overnight dialysis at 4 °C in 0.2M sodium acetate buffer (pH = 5). At last, ARC1172 and SpyTag were mixed at a 1 : 10 molar ratio of aptamer to SpyTag at room temperature

overnight to achieve the conjugation. A slide-A-Lyzer MINI Dialysis device with 7K Molecular Weight Cut Off (MWCO), (Thermo Fisher Scientific) was utilized to filter the conjugate from the extra unbonded SpyTag. The aptamer-SpyTag conjugate was validated by gel electrophoresis (Fig. S1A†).

Parallelly, a DNA handle was produced and conjugated to i-27 SpyCatcher (a kind gift from Dr Mark Howarth at the University of Cambridge). Polymerase Chain Reaction (PCR) was employed using Vent DNA polymerase (New England Biolabs, Ipswich, MA) in the presence of 20 mM DTT to produce the DNA handle as described previously.⁴⁰ The pGEMEX 1 plasmid DNA (Promega, Madison, WI) was utilized as the template. Additionally, two primers were used: 5'-thiol-modifier-C6-SS-CGA-CGA-TAA-ACG-TAA-GGA-CAT-C and 5'-biotin-CAA-AAA-ACC-CCT-CAA-GAC-CC. The thiol group of the DNA handle was reduced with DTT and then activated with DTDP right before conjugation with SpyCatcher. Simultaneously, the thiol group on the cysteine of the i-27 SpyCatcher was reduced by DTT at room temperature for 1 hour at a 1 : 10 molar ratio of SpyCatcher to DTT. The SpyCatcher solution was then purified from DTT by Zeba spin desalting columns (Thermo Fisher Scientific). Subsequently, the DNA handle and SpyCatcher were mixed at a 1 : 1 molar ratio at room temperature overnight to achieve the conjugation. Conjugation results were confirmed by gel electrophoresis (Fig. S1B†).

The i-27 SpyCatcher, with its relatively high molecular weight (~32.3 kDa), was primarily utilized in the validation

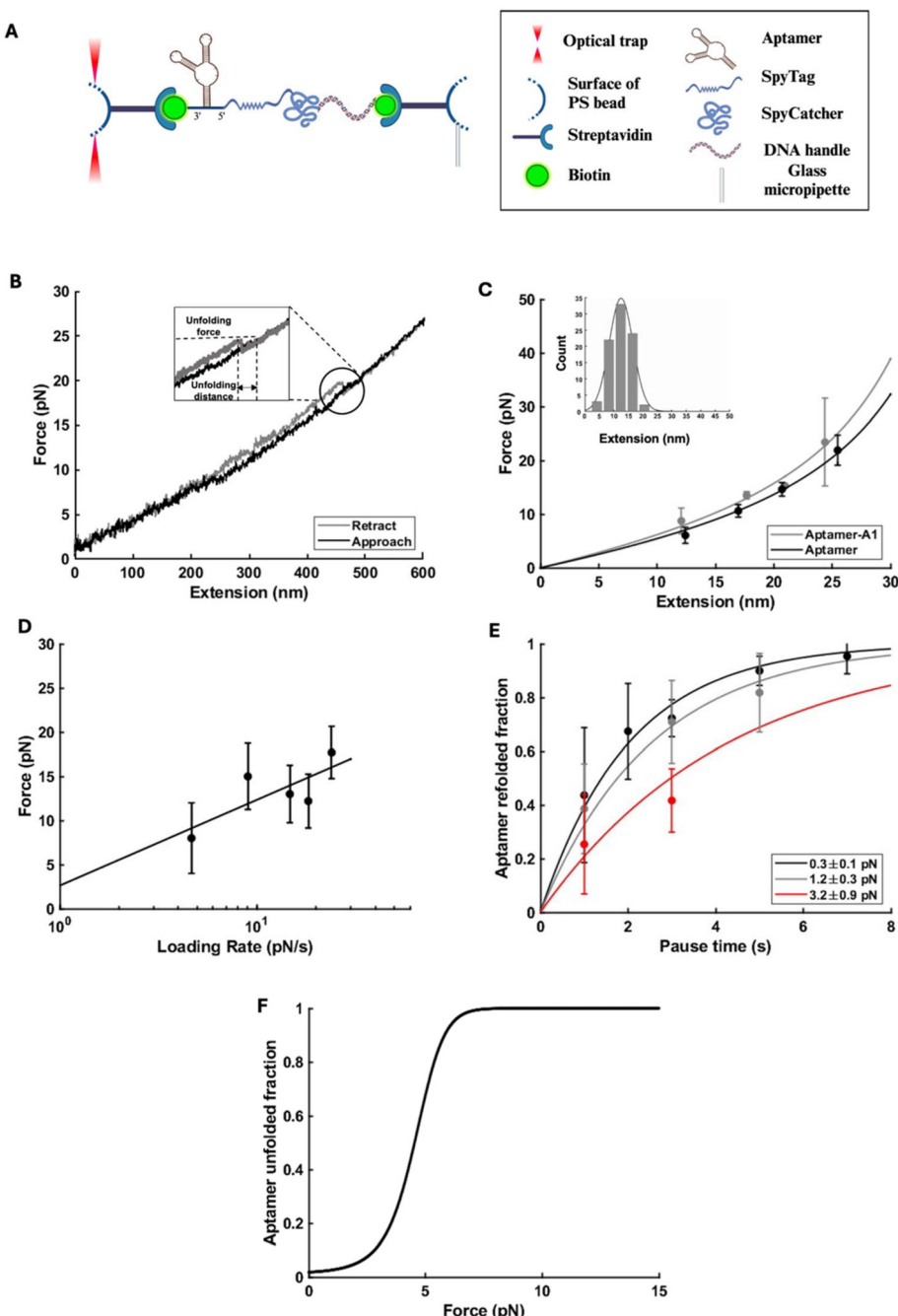


Fig. 2 Mechanical properties of aptamer ARC1172 measured by optical tweezers. (A) Schematics of the single-tether construct used in the setup of optical tweezers to test aptamer unfolding and refolding. (B) Force vs. extension pulling curve of the aptamer. The dip in the retract curve represents an unfolding event that is enlarged in the inset. (C) Worm-like chain (WLC) fit (eqn (1)) of the unfolding results for aptamers in the absence (black curve) and presence of A1 (grey curve). The extension distances were sorted by unfolding force and a histogram of each bin (inset) was fit to a Gaussian (inset, solid line) to find peak extension and force average for that bin. Data from histograms were plotted as unfolding force vs. extension (dots in the plot) and fitted by the worm-like chain model (lines in the plot) to extract the persistence and contour length of the aptamer. (D) The most probable unfolding forces plotted against their corresponding loading rates. The solid line is a linear fit of the data to the Bell-Evans model (eqn (4)), from which the unfolding rate in absence of force, k_u^0 , and the distance to the transition state, γ , were obtained as fitted parameters. By incorporating these fitted parameters into eqn (2), the unfolding rate as a function of force $k_u(f)$ was obtained. (E) Fitting of the refolding fraction. Aptamer refolded fraction at varying pause times under different forces were fitted into a first order reaction equation, from which the refolding rate as a function of force $k_f(f)$ was obtained as the slope of the linear fit. Fitting the reaction rate as a function of force $k_f(f)$ and the corresponding force values into eqn (5) gave the refolding rate of aptamer in absence of force, k_f^0 , as well as the compliance, κ , of the unfolded aptamer as fitted parameters. (F) The expected unfolded fraction of ARC1172 at steady state as a function of pulling force. Employing the generated unfolding rate, $k_u(f)$ from eqn (2) and the refolding rate, $k_f(f)$ from eqn (5) into eqn (6), aptamer unfolded fraction as a function of force was obtained.

experiments. Its use aimed to observe a noticeable shift in the electrophoresis bands, confirming the aptamer-SpyTag conjugation through the specific binding between SpyTag and SpyCatcher, as well as to confirm the shift in bands between the DNA handle-SpyCatcher conjugate and the unconjugated DNA handle. However, for the construction of the SMORES construct, Cys-SpyCatcher was employed. The Cys-SpyCatcher protein was generated using Plasmid Cys-SpyCatcher002 (Addgene, Watertown, MA), following the protein expression method outlined in the literature.⁴¹

Subsequently, the surface of 1 μm -diameter carboxyl polystyrene beads (Polysciences, Warrington, PA) was covalently modified with 1-ethyl-3-(3-dimethylaminopropyl) carbodiimide hydrochloride (EDAC, Polysciences). This modification introduced an active ester that was reactive with the primary amines on the streptavidin protein (Sigma Aldrich) resulting in a covalent bonding of the beads with streptavidin. One batch of the streptavidin-beads was incubated with biotinylated aptamer linked to SpyTag. The other batch was incubated with biotinylated DNA handle linked to SpyCatcher.

It should be noted that, although a disulfide covalent interaction was used on the 5' end of the aptamer to connect it with the DNA handle, a non-covalent bond (biotin-streptavidin) was used to connect the aptamer on the 3' end with one of the two beads in the single tether structure used in the optical tweezers chamber. However, this interaction is still stronger than those from the intramolecular base pairing, allowing the aptamers to stretch without breaking off from the beads. The binding energy of the biotin and avidin approaches that of a covalent bond,⁴² which requires much more energy to break than unzipping the internal base pairing in the aptamers.⁴³

In the optical tweezers experiments (Fig. 2A), one bead was aspirated by the micropipette tip, while the other bead was captured and controlled by a laser trap. By aligning the two beads and moving them toward each other to contact for a few seconds, the SpyTag and the SpyCatcher would interact and form a tether between the two beads during the pulling process, allowing measurement of unfolding behavior of the aptamer. Force and bead-to-bead distance were recorded at different loading rates. The force-extension data were fitted to the wormlike chain (WLC) model (eqn (1))⁴⁴ where (F) is the applied force, x refers to the end-to-end distance of the biopolymer being stretched, k_B represents the Boltzmann's constant, and L_p and L_c are the persistent and contour lengths, respectively:

$$\frac{F(x) \cdot L_p}{k_B T} = \frac{1}{4} \left(1 - \frac{x}{L_c} \right)^{-2} - \frac{1}{4} + \frac{x}{L_c} \quad (1)$$

Unfolding of the aptamer in the presence of A1 was further analyzed using the Bell-Evans model,⁴⁵ initially devised to explain the influence of external forces on the unfolding rates of proteins. In this instance, the model was adapted for the unfolding of aptamers in presence of their ligand, the VWF-A1 domain. According to this model, a pulling force, f , distorts

the intramolecular bonding of the aptamer, leading to a lower activation energy and an increase in the unfolding rate, $k_u(f)$

$$k_u(f) = k_u^0 \exp\left(\frac{f\gamma}{k_B T}\right) \quad (2)$$

where k_u^0 is the unfolding rate constant in the absence of a pulling force, γ is the distance to the transition state, k_B is the Boltzmann constant, and T is the absolute temperature. For a constant loading rate R_f , the probability of the unfolding of the complex as a function of the pulling force f is given by:

$$p(f) = k_u^0 \exp\left(\frac{f\gamma}{k_B T}\right) \exp\left\{ \frac{k_u^0 k_B T}{\gamma R_f} \left[1 - \exp\left(\frac{f\gamma}{k_B T}\right) \right] \right\} \quad (3)$$

The most probable unfolding force is given by (eqn (4)). Hence, the Bell model predicts that the most probable unfolding force, f^* , is a linear function of the logarithm of the loading rate. This equation was used to fit the most probable unfolding forces of the aptamer *versus* $\ln(R_f)$.

$$f^* = \frac{k_B T}{\gamma} \ln\left\{ \frac{\gamma}{k_u^0 k_B T} \right\} + \frac{k_B T}{\gamma} \{ \ln R_f \} \quad (4)$$

In most instances, the refolding of ARC1172 is not readily apparent in relaxation traces. However, following a specific relaxation period (*i.e.*, paused time) at low forces (0.3–3 pN) for varying durations, subsequent pulling traces revealed the reappearance of unfolding. This observation suggested a potential occurrence of refolding during the relaxation phase. To explore the force dependence of refolding, fractions of refolded aptamers at varying pause times were fitted to a folding reaction time constant $\tau \sim \exp(f^2)$ where the refolding rate as a function of force, $k_f(f)$ is represented by eqn (5):

$$k_f(f) = k_f^0 \exp\left(\frac{-f^2}{2\kappa k_B T}\right) \quad (5)$$

where k_f^0 is the refolding rate in the absence of force, κ is the compliance of the unfolded molecule, k_B is the Boltzmann constant, and T is the absolute temperature. This model was developed by E. Evans⁴⁶ and accounts for the soft compliance of the unfolded state. Additionally, using the force-dependent kinetic rates, unfolding rate, $k_u(f)$ from eqn (2) and refolding rate, $k_f(f)$ from eqn (5), the unfolded fraction of the aptamer at steady state as a function of force was calculated using the following formula (eqn (6)):

$$\text{Aptamer unfolded fraction} = \frac{k_u(f)/k_f(f)}{1 + k(f)/k_f(f)} \quad (6)$$

2.2 Labelling of the VWF-A1 domain

Recombinant VWF-A1 (residues 1261–1468, ImmunoPrecise Antibodies, Oss, Netherlands) was used as the target in the aptamer-based SMORES construct. The release of A1 at defined shear values and its functionality post-release, particularly in terms of binding to GPIb, were characterized to demonstrate the shear response of the construct.

For the single molecule flow experiments to quantify the release of A1, the VWF-A1 domain was labeled with Quantum

Dots (QDs, emission wavelength 600 nm) using the carboxyl quantum dots protein conjugation kit (Ocean NanoTech, San Diego, CA). To achieve the QDs-A1 coupling, 12.5 μ L of the QDs solution was diluted by 87.5 μ L of the reaction buffer (50 mM MES, pH 5.2; 0.05% Proclin 300, Polysciences) followed by addition of 400 μ L of 1 mg ml^{-1} A1. Afterwards, 2.8 μ L *N*-ethyl-*N*-dimethylaminopropyl-carbodiimide (EDC, Polysciences) at 10 mg ml^{-1} was added to the QDs-protein mixture and incubated for 2 h at room temperature. The QD-protein conjugate was then washed and filtered from unconjugated A1 using 30k MWCO Pierce concentrator (Thermo Fisher Scientific). The washing and storing buffer (Polysciences) consisted of 10 mM Tris (pH 8.0) supplemented with 0.05% bovine serum albumin (BSA, Sigma Aldrich), and 0.05% Proclin 300.

For the ELISA assay used to test the binding of the released A1 to GPIB, the VWF-A1 domain was labeled with biotin using an EZ-Link Sulfo-*N*-Hydroxysuccinimide (NHS)-LC-Biotinylation Kit (Thermo Fisher Scientific). A 10 mM Sulfo-NHS-LC-Biotin solution was immediately prepared before use. 88 μ L of the biotin solution was added to a 1 ml of 1 mg ml^{-1} A1 in 0.01M phosphate-buffered saline (PBS, Thermo Fisher Scientific) to achieve a 20-fold molar excess of biotin reagent to protein following the guidelines outlined in the kit's data sheet. The mixture was incubated at room temperature for 1 h. The conjugate was purified from excess biotin using a 7 kDa MWCO Zeba desalting column.

2.3 Construction of the aptamer-based SMORES material

The construction of the SMORES material was achieved by conjugating thiolated ARC1172 aptamer molecules with 1 μ m-diameter amine polystyrene beads (Polysciences) using the *N*- γ -maleimidobutyryl-oxysuccinimide ester (GMBS) crosslinker

(Thermo Fisher Scientific) (Fig. 3A). The beads were first incubated with the GMBS crosslinker at a 1 : 10⁶ molar ratio for 30 minutes at room temperature so the amine groups on the surface of the beads reacted with the oxysuccinimide ester in GMBS. The GMBS-coated beads were then washed twice in 0.01 M PBS using centrifugation to remove excess cross-linker molecules. Simultaneously, the disulfide bonds between the aptamer ARC1172 dimers were reduced with DTT at room temperature for 1 hour at a 1 : 10 molar ratio of aptamer to DTT. Simultaneously, EDTA was simultaneously added to the mixture as previously described. The aptamer solution was then purified from excess DTT and EDTA using Micro Bio-Spin chromatography columns, and the buffer was exchanged with 0.01 M PBS. After the reduction step, the aptamer solution was incubated with the GMBS crosslinker-coated beads for 30 minutes at room temperature at a 1 : 50 molar ratio to attain the reaction between the sulphydryl end of the aptamer and the maleimide reactive group of the cross-linker, thereby achieving the conjugation between the aptamer and the 1 μ m-diameter beads. The aptamer-coated beads were then pelleted down by centrifugation, and the supernatant was discarded. The pellet of beads was re-suspended in 10 mg ml^{-1} BSA in 0.01 M PBS and incubated for 30 more minutes at room temperature. Finally, the beads were washed in 10 mg ml^{-1} BSA in 0.01 M PBS and were subsequently pelleted down by centrifugation. Following this, the beads were stored in 1 ml of 0.01 M PBS, pH 7.4, containing 10 mg ml^{-1} BSA, 0.1% NaN₃ (Sigma-Aldrich), and 5% glycerol (Sigma Aldrich).

An ELISA assay was performed to quantify the number of bound aptamers per bead through detecting the biotin at the 3' end of the aptamer. To attain this, samples of aptamer-coated beads were blocked with 10 mg ml^{-1} fatty acid-free BSA

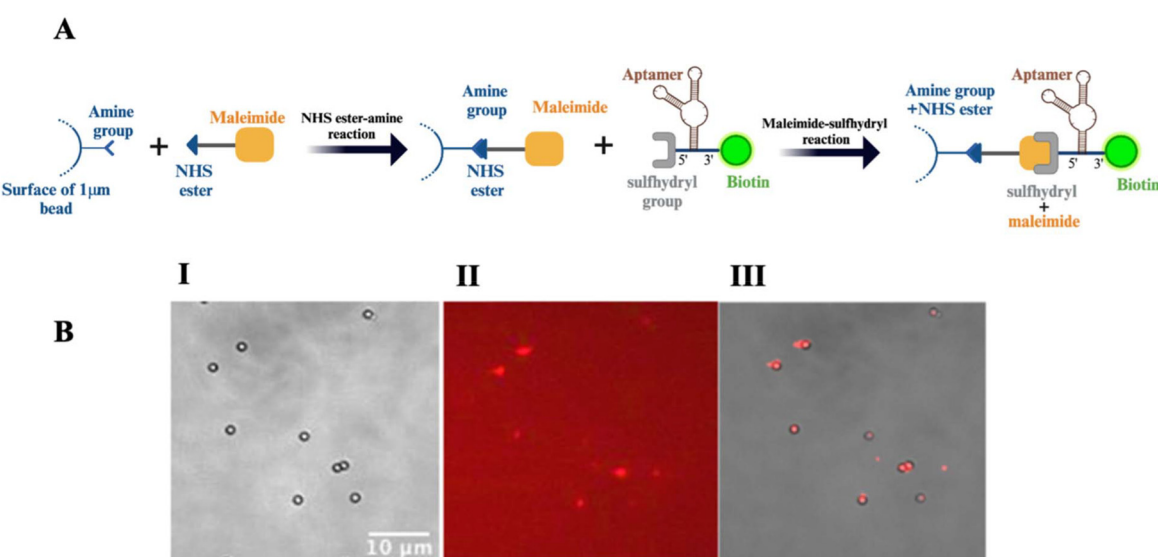


Fig. 3 Construction of the aptamer-based conjugate and images of the SMORES construct and its specific binding with VWF-A1 in a microfluidic channel. (A) Schematics of the process used to construct the aptamer based SMORES material, which was used in the flow experiments. (B, I) A bright field image showing the SMORES construct (1 μ m aptamer coated beads) immobilized in the microfluidic channel. (B, II) Fluorescent signals from QDs-labeled VWF-A1 binding to the channel captured by TIRF microscopy. (B, III) Co-localization of the amine beads and the fluorescently labeled A1 made by overlaying the two images in (A) and (B) confirming specific binding of A1 to the SMORES constructs.

(Sigma Aldrich) for 1 hour and then reacted with streptavidin-horseradish peroxidase conjugate (SA-HRP, 1:200 dilution, Fisher Scientific, Pittsburgh, PA) for 1 hour at room temperature for biotin quantification. Following this, the HRP-bead sample was reacted with 100 μ L of 3,3',5,5'-Tetramethylbenzidine, (TMB, Sigma-Aldrich). After incubation for 30 min, the beads were pelleted down and the supernatant containing the colorimetric products was mixed with 100 μ L of the ELISA stopping solution (Thermo Fisher Scientific). Absorbances were measured at 480 nm using a Tecan plate reader. All dilutions were done with 10 mg mL^{-1} fatty acid-free BSA in 0.01 M PBS and all incubations were performed at room temperature. To generate the standard curve, some wells of the 96-well plate were pre-coated in parallel with 2 μ M streptavidin and blocked with 10 mg mL^{-1} fatty acid-free BSA, followed with addition of a series of serial dilutions of Bis dPEG biotin (Quanta BioDesign, Plain City, OH) ranging from 10 nM to 2 μ M. After incubation for 2 hours, SA-HRP was added and incubated with the wells. After washing the plate three times, 100 μ L TMB was added to the sample wells for 30 min before the reaction was stopped by adding 100 μ L of the ELISA stopping solution. Absorbances for the standard wells were measured at 480 nm using a Tecan plate reader.

2.4 Microfluidic device fabrication

The microfluidic device and the channel pattern used in the experiment are illustrated in Fig. 1B. The dimensions of the channel were 50 μ m in height, 8 mm in length, and 1.0 mm in width. The microfluidic channel was fabricated on a silicon wafer using standard photolithography techniques. Using the wafer as a mold, a mixture of polydimethylsiloxane (PDMS) precursor and curing agent (Dow Corning, Midland, MI) in a ratio of 5 : 1 was incubated at 60 $^{\circ}$ C overnight to completely cure. Inlets and outlets were drilled through the solidified PDMS layer, which was then sealed onto a #1.5 glass coverslip (Corning, Corning, NY) by oxygen plasma.

2.5 Surface modification and the immobilization of the SMORES material

The immobilization process of the SMORES conjugate onto the glass surface of the microfluidic channel happened through a series of sequential steps. First, after device fabrication, the glass surface of the microfluidic channel was functionalized with 100 μ g mL^{-1} biotinylated BSA (Sigma-Aldrich) for 2 hours. Then, a commercial blocking solution (Candor, Wangen, Germany) was injected into the channel and incubated for 30 min. Following the blocking step, the channel was washed with 0.01 M PBS. Afterwards, 100 μ g mL^{-1} streptavidin was injected, and the device was incubated for 15 min before the channel was washed again by PBS. Subsequently, the solution of aptamer-coated beads was slowly injected into the channel and incubated for 30 min, during which the 5'-end biotin of the aptamer bound to streptavidin. After washing the channel to remove unreacted beads, QDs-A1 in 0.01 M PBS was injected into the device and incubated for another 10 minutes. All incubations occurred at room temperature. To minimize

non-specific binding, the commercial blocking solution was used to dilute the reagents to the desired concentrations.

2.6 Flow experiment and quantification of the released A1 by fluorescence intensity

To investigate flow modulation of the function of the SMORES construct, a syringe pump was used to apply variable flow rates ranging from 20 to 100 μ L min^{-1} to the microfluidic channel immobilized with the SMORES-A1 pair. The aptamer-A1 interaction was observed through Total Internal Reflection Fluorescence Microscopy (TIRFM; Nikon Ti, 100 \times objective, 1.49 N.A.). Subsequently, image analysis was conducted using ImageJ to evaluate the co-localization of aptamer-coated beads and QDs-A1.

In order to assess the aptamer's ability to unfold and release its ligand A1, flow-through samples containing QDs-A1 were collected at each flow rate, and the fluorescence intensity was determined for the outflow samples using excitation at 480 nm and emission at 600 nm. This technique enabled the characterization of A1 release as a function of the flow rate, facilitating the evaluation of the critical flow rate at which the ARC1172 aptamer undergoes conformational changes and liberates its ligand. The flushing buffer used in this flow experiment was based on 0.01M PBS and contained 0.02% Tween 20 (Fisher Scientific, NH), 0.1 mM free biotin (Sigma-Aldrich), and 0.5 mg mL^{-1} BSA.

2.7 Function of the released A1 by ELISA

It has been well established that VWF binds with the platelet receptor, GPIB, through the VWF-A1 domain. An ELISA assay was performed to test the functionality of the released A1 through its binding with GPIB. This was done by reacting the VWF-A1 domain from the flow-through samples with surface-immobilized GPIB protein. In this study, biotinylated A1 was loaded onto SMORES, and the flow-through samples under variable flow conditions (10–100 μ L min^{-1}) were collected. GPIB (Sino biological, Wayne, PA) at 2 μ M was incubated with a 96-well plate for 2 hours. After blocking the plate with 10 mg mL^{-1} fatty acid-free BSA, the flow-through samples containing the released A1 from the microfluidic devices were added to the GPIB-coated plate. Simultaneously, the ELISA calibration curve was attained by reacting the GPIB wells with a serial dilution of biotinylated A1 ranging from 10 nM to 0.5 μ M for 1 hour. After washing the plate with ELISA wash buffer (Thermo Fisher Scientific), streptavidin-HRP conjugate diluted 1 : 200 was used to react with biotinylated A1 molecules. After washing the plate three times, TMB was added to the samples before the reaction was stopped by adding 100 μ L of the ELISA stopping solution. Following stopping the reaction, absorbances were measured at 450 nm using a Tecan plate reader. All dilutions were done in 10 mg mL^{-1} fatty acid-free BSA and all incubations were performed at room temperature.

2.8 Statistical analysis

Over 300 force curves were recorded for each pulling speed in Fig. 2 and S2.[†] Curve fitting was performed using IGOR Pro or

MATLAB software by minimizing the chi-squared statistics for the optimal fit. Eight independent microfluidic chips ($n = 8$) were used to test the A1 release at different flow rates for the A1 release data reported in Fig. 4. The quantified absorbance, indicating the release of QDs-A1 from each device, was normalized using max-min normalization. The results were reported as the mean \pm standard error of the mean. Seven chips ($n = 7$) were used for the data reported in Fig. 5A. The data in Fig. 2C–E, S2C,† Fig. 4 and 5A were reported as the mean \pm the standard error of the estimate.

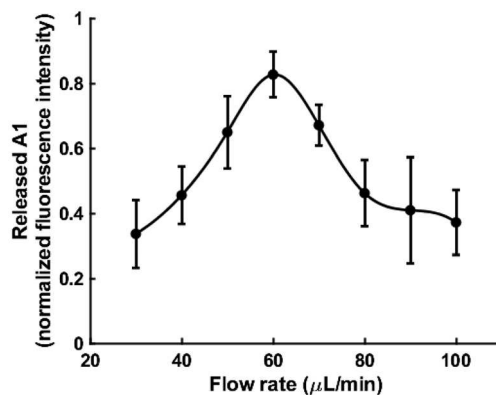


Fig. 4 Normalized fluorescence intensity of flow-through samples plotted as a function of flow rate. The graph shows a peak fluorescence reading at $60 \mu\text{L min}^{-1}$ indicating the threshold flow rate at which QDs-labeled A1 is released. 8 independent microfluidic devices were used for the flow experiments and each subjected to stepwise flow rates from 20 to $100 \mu\text{L min}^{-1}$.

3. Results and discussion

3.1 Unfolding and refolding of aptamer ARC1172 by single molecular force measurements

In the context of inhibiting VWF-induced platelet activation and thrombosis, several aptamer designs targeting the VWF A1 domain have been investigated. These include ARC1172 ($\text{KD} = 326 \text{ pM}$),³⁷ a natural base DNA aptamer; ARC1779 ($\text{KD} = 2 \text{ nM}$),³⁴ a 2'-OMe RNA/DNA aptamer; TAGX-0004 ($\text{KD} = 2.2 \text{ nM}$);³⁵ and Rn-DsDsDs-44 ($\text{KD} = 75 \text{ pM}$),³⁶ a DNA aptamer with an artificial hydrophobic base analogue. All of these aptamers have been shown to inhibit VWF-dependent or shear stress-induced platelet aggregation and adhesion to collagen-coated matrices.

ARC1172 was selected for our construct due to its ease of synthesis, the favorable safety profile of its derivative ARC1779 in Phase 1 clinical trials,³⁴ and the extensive literature on its crystal structure and interactions with the VWF A1 domain,^{37,39} which provided a solid foundation for our work.

In order to characterize the mechanical properties of the aptamer ARC1172 as a molecular force transducer, we first used optical tweezers to study the aptamer's unfolding behavior. This was achieved by measuring the aptamer's unfolding extension under different loading rates and pulling forces while the aptamer was connected between two beads captured by a laser trap and a micropipette respectively (Fig. 2A). Overstretching of the DNA handle was observed during the pulling experiments, which was indicated of the formation of a single tether between the microbeads. A typical force *vs.* extension curve is shown in Fig. 2B. Aptamer unfolding was

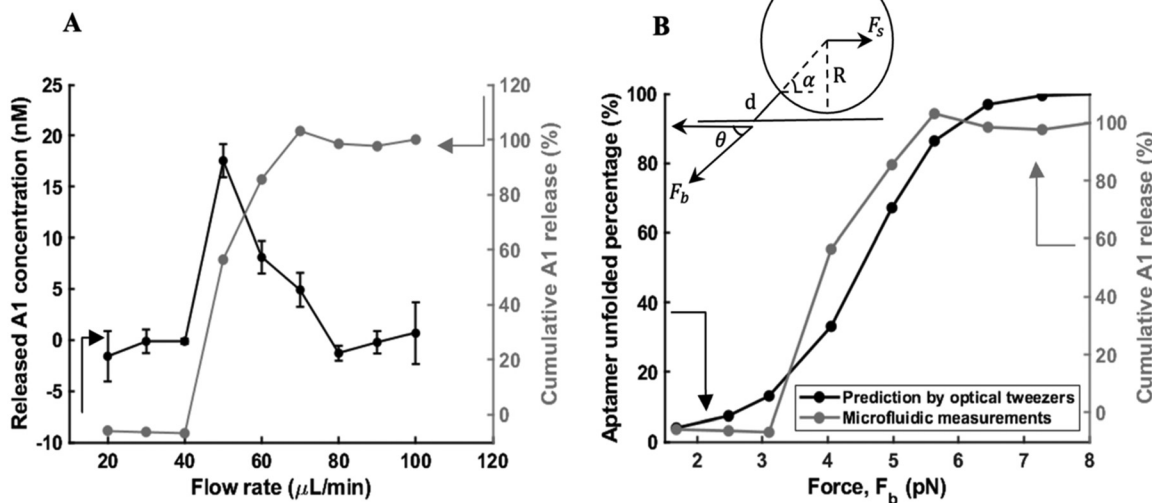


Fig. 5 Quantification of the released A1 based on binding with GPIB and correlation with results from the single-molecule force microscopy experiments. (A) Concentration of GPIB bound A1 plotted as a function of flow rate (black curve) and the percentage of cumulative A1 release (grey curve) reveal a narrow range of threshold flow rates of $40\text{--}80 \mu\text{L min}^{-1}$, within which A1 was released and was function in GPIB binding. (B) The comparison of the unfolded percentage of the aptamer at steady state (black curve) predicted by optical tweezers measurements, along with the percentage of cumulative A1 release as a function of force on the tether, F_b (grey curve), demonstrates a consistent trend. The force on the tether, F_b , was calculated according to a model described previously (inset in Fig. 5, adapted from Chen *et al.*)⁶¹

marked by a drop in force and an abrupt increase in the length of the tether between the two beads in the retract curve (Fig. 2B, inset). The unfolding event captured in the example plot happened at 19.85 pN with a 21.80 nm unfolding distance under a pulling speed of 400 nm s⁻¹ and a loading rate of 3.33 pN s⁻¹. The force range for ARC1172 unfolding is comparable to those reported in the literature. Previous studies on the unfolding dynamics of DNA strands containing hairpin structures such as 20R55/4T found the unfolding occurring around \approx 13 pN.⁴⁷ Studies on lambda phage DNA observed unzipping (and re-zipping) events at forces between 10 and 15 pN.⁴⁸

Over 300 unfolding events were observed, and the unfolding forces and distances were recorded from the force *vs.* extension-retract curves and fitted into a worm-like chain (WLC) model (eqn (1)). The fitting (Fig. 2C) yielded a persistence length, L_p of 0.31 ± 0.032 nm, and a contour length, L_c of 45.10 ± 2.16 nm with the aptamer alone (black curve). In order to compare the mechanics of the aptamer ARC1172 with and without its ligand, similar single-molecular tests were conducted on aptamer in the presence of the VWF-A1 domain in the reaction chamber. Fitting this set of data into a WLC model (eqn (1))⁴⁴ generated an L_p of 0.24 ± 0.078 nm and an L_c of 46.88 ± 7.97 nm (grey curve). The persistence length and contour length for both unfolding experiments of the aptamer, with and without A1, were not found to be significantly different. The yielded contour lengths measured from both experiments match well with our prediction of 45 nm, considering there are 75 bases of DNA in the aptamer structure and the distance between successive ssDNA phosphorus is \sim 6 Å.⁴⁹ Comparable persistent lengths indicate that the mechanical properties of aptamer ARC1172 remain unaltered by the interaction with the ligand, *i.e.*, association of A1 does not enhance the mechanical stability of the aptamer, at least when tensile force is applied *via* the 5' and 3' ends of the aptamer. Unfolding of the aptamer in the presence of A1 was further analyzed using the Bell-Evans model.⁴⁵ Over a range of force loading rates, the most probable unfolding force was determined and plotted against the logarithm of the loading rate according to eqn (4). The fitting (Fig. 2D) yielded an unfolding rate of aptamer in the absence of force to be $k_u^0 = 0.13 \pm 0.14$ s⁻¹.

The aptamer-based conjugate was engineered for immobilization onto the surface of a microfluidic channel, enabling the examination of its structure and function under physiologically relevant flow conditions. Recognizing that the immobilized aptamers would be exposed to a fixed flow/shear force in the microfluidic environment rather than continuously increasing force loading, optical tweezers were employed to further explore the conformational behavior of the aptamer under conditions that mimic those in the microfluidic environment. The two beads tethered by the aptamer were subjected to force clamping in the presence of A1 at different fixed force levels for a certain relaxation period (pause time). At low forces (0.3–3 pN) for varied durations, unfolding was observed again in some cases in the subsequent pulling traces, indicating that refolding may have occurred during the relaxation period. The force dependency of refolding (Fig. 2E) was fitted

using the maximum likelihood to an f^2 model (eqn (5)), which takes into account the soft compliance of the unfolded state using a model developed by Evans *et al.*⁴⁶ This model has been previously employed to describe the refolding of various protein domains.⁴⁰ The fitting process yielded a refolding rate $k_f^0 = 0.48 \pm 0.07$ s⁻¹, in the absence of force, and the compliance of unfolded aptamer $\kappa = 1.7 \pm 0.4$ pN nm⁻¹. Furthermore, using the force-dependent kinetic, the unfolding rate $k_u(f)$ from eqn (2) and refolding rate $k_f(f)$ from eqn (5), the unfolded fraction of the aptamer at steady state as a function of pulling force was predicted by eqn (6) (Fig. 2F). The predicted fraction of unfolded aptamer ARC1172 starts to escalate when the force is above 2 pN, reaching saturation around 7 pN. This suggests a narrow range of threshold forces of 2–7 pN, centered at approximately 5.5 pN, that trigger a rapid shift in the aptamer conformation from a folded to an unfolded state.

In the literature, the melting temperature is the commonly used indicator of DNA and RNA structural stability,⁵⁰ which can be used to infer the unfolding energy. In fact, models to predict the temperature and energy of melting DNA secondary structures have been well developed.^{51,52} Here, optical tweezers were selected to study aptamer unfolding due to their single-molecule sensitivity, precise force control, and real-time monitoring, allowing direct observation of mechanical unfolding events at the individual molecule level.⁵³ The versatility of optical tweezers makes them well-suited for capturing the force-dependent mechanical behavior of aptamer ARC1172. Utilizing this approach provides predictions for the expected force range at which the payload for ARC1172 is released under constant shear, which has been validated in the rest of the paper.

3.2 Binding of aptamer ARC1172 with A1 by single molecular force measurements

Previous studies by X-ray crystallography demonstrated that the interaction of ARC1172 with the A1 domain encompasses 16 of the aptamer's bases. Fourteen of these bases form 24 hydrogen bonds and 4 salt bridges with the A1 domain. Additionally, two unpaired bases that do not participate in base-base stacking are stabilized by the A1 domain. Specifically, the thymine base of T10 extends from stem II to stack with Phe603's aromatic ring, while the cytosine base of C29 interacts with seven amino acid residues in the A1 domain: Gln625, Pro655, His656, Ala657, Asn658, Leu659, and Lys660.^{37,39} Here we employed optical tweezers to precisely quantify the binding affinity and interactions between the aptamer and the A1 domain.

Over 700 binding rupture events were captured between ARC1172 and A1 under different pulling speeds from 50 to 500 nm s⁻¹. The rupture force is in the range of 12–30 pN, dependent on the loading rate. The force range is consistent with the literature, which documents that unbinding forces between single ligand-receptor pairs can range from a few pico-Newton to over 50 pN.⁵⁴ Specifically, regarding the unbinding forces between aptamers and their ligands, studies

have reported values as high as 39 pN (ref. 55) and as low as 4.45 pN.⁵⁶

Employing the Bell Evans fit⁴⁵ (eqn (4)) on the unbinding data (Fig. S2†), the dissociation rate between aptamer ARC1172 and the VWF-A1 domain in the absence of force is estimated to be $0.0089 \pm 0.0052 \text{ s}^{-1}$. This indicates that ARC1172 and the A1 domain have high affinity, consistent with the literature,³⁷ and minimizes the spontaneous release of the payload without an appropriate flow trigger. The Bell-Evans model⁴⁵ has been previously employed to study the dissociation rate between protein–ligand interactions, providing valuable insights into their binding dynamics. For example, the study by Deng *et al.* (2012)⁵⁷ elucidates the streptavidin–biotin interaction, revealing an exceptionally high affinity with a dissociation rate in absence of force of $5.4 \times 10^{-6} \text{ s}^{-1}$.

Many methods have been employed to evaluate the binding affinity of receptors and ligands, including isothermal titration calorimetry (ITC),⁵⁸ which measures heat changes upon binding to determine thermodynamic parameters; surface plasmon resonance (SPR),⁵⁹ which measures changes in reflected light intensity to determine kinetic and affinity parameters; and microscale thermophoresis (MST),⁶⁰ which measures the differential diffusion rates of aptamer-target complexes. In the context of investigating binding and unbinding processes at the single-molecule level, optical tweezers emerge as a powerful and versatile technique due to their precision, sensitivity, and ability to control the applied force to be relevant to the molecule of interest. They also allow for the application of low forces or loading rates to stretch molecules, facilitating the recording of unfolding and folding processes close to equilibrium transitions, thereby accurately capturing the dynamic interactions and subtle conformational changes in the aptamer–ligand complex.

3.3 Immobilization of the aptamer based SMORES construct and A1 capture by SMORES

Following the characterization of its mechanical response and validation of its ligand binding, ARC1172 was conjugated onto polystyrene beads to build the SMORES construct. Based on the data sheet from the manufacturer, the polystyrene (PS) beads are spherical particles with a uniform size and smooth surface. The average diameter is 0.92 microns, within a range of 0.90 to 1.10 microns. Amine functionalized polystyrene beads were chosen for their ease of functionalization, enabling efficient incorporation into the aptamer-based construct. They are generally biocompatible when properly modified. For *in vivo* applications, modifications such as PEGylation can be employed to further enhance their biocompatibility. Additionally, polystyrene beads exhibit precise size control and uniformity, which are critical for ensuring consistent performance as a shear sensor in circulation. Finally, their stability and favorable optical properties also render them suitable for therapeutic applications and imaging. The SMORES material was constructed by linking the 5' thiol group of the ARC1172 molecules with 1 μm-diameter amine polystyrene beads *via* the GMBS (*N*-γ-maleimidobutyryl-oxysuccinimide ester) crosslinker (Fig. 3A).

To characterize the density of aptamers immobilized on each bead, an ELISA assay was used to quantify biotin groups on the beads, as each aptamer molecule presents one biotin on the 3' end. The density was found to be 6.52×10^4 aptamer molecules per bead.

Employing the microfluidic device shown in Fig. 1B, we next immobilized the SMORES construct onto the surface of a micro-channel to characterize its capability to immobilize VWF-A1 using TIRF microscopy. The channel was first functionalized with streptavidin to specifically bind the construct containing biotinylated aptamers, followed by saturating the free streptavidin binding sites on the surface with free biotin. The concentration of each reagent was optimized to minimize non-specific binding. The 1 μm beads were visible with bright-field illumination (Fig. 3B, I). Incubating QDs-A1 with the immobilized beads followed by rinsing resulted in fluorescent signals from A1 (Fig. 3B, II), which co-localized with the beads (Fig. 3C, III). This indicates the binding of the VWF-A1 domain to the ARC1172 aptamer molecules on the surface of the beads. In a control experiment without flowing QDs-A1, no fluorescent signals were observed in the channel. Alternatively, a channel without the SMORES construct captured little QDs-A1, confirming that the detected fluorescent signals were the result of QDs-A1 specifically binding to the aptamer molecules located on the bead's surface.

3.4 Release of A1 under flow

Following confirmation of the specific interaction between SMORES and A1, modulation of the structure and function of SMORES was further inspected by characterizing A1 release under varying flow conditions. A syringe pump was used to apply 9 different flow rates stepwise from 20 to 100 $\mu\text{L min}^{-1}$. An equal volume of each flow-through sample (120 μL) was collected from the microfluidic device by adjusting the duration of flow at each condition. The fluorescence intensity at 600 nm of the collected flow-through samples was measured, indicative of the concentration of QDs-A1 within the samples. Plotting the normalized fluorescence intensity of the flow-through samples against flow rate revealed an elevation in A1 release, commencing at a flow rate of 40 $\mu\text{L min}^{-1}$ and peaking at approximately 60 $\mu\text{L min}^{-1}$ (Fig. 4). This peak release suggests that at a flow rate of approximately 60 $\mu\text{L min}^{-1}$, the drag force experienced by the bead induced a significant conformational change in most of the aptamer molecules, which modulated the bioavailability of the VWF-A1 domain, and ultimately resulted in the release of most of the aptamer-bound A1. As flow rates further increased in the same device, the remaining bound A1 molecules were progressively released. Since most of the A1 was released at 60 $\mu\text{L min}^{-1}$, the remainder A1 release beyond 60 $\mu\text{L min}^{-1}$ was less than the peak, as indicated by the reduced normalized fluorescence intensity on the plot. The data point at 20 $\mu\text{L min}^{-1}$ was excluded from the plot, as free A1 from the loading step was flushed from the microfluidic device during this initial flow condition, leading to a high fluorescence intensity, which doesn't accurately reflect flow modulation of the SMORES construct to deliver its

payload A1. It is also worth noting that not all A1 were releasable from the SMORE construct, as observed from fluorescence imaging of the microfluidic device after the flow experiments. This is due to the high density of aptamers on each microbead, while only a few of the aptamers bridge the microbeads and the substrate. These bridging aptamers are the ones that could be loaded at low shear and deliver the payload upon subsequent high shear exposure. The aptamers not tethered to the surface can bind A1 but don't unload A1 at high shear.

It has been well established that the VWF-A1 domain forms the principal binding site for the platelet glycoprotein Ib (GPIB) receptor.²⁰ Building on this knowledge, an ELISA assay was carried out to assess the function of the released A1 at binding to GPIB in flow-through samples collected at different flow rates (10–100 $\mu\text{L min}^{-1}$). As seen in Fig. 5A, released A1 bound to GPIB rose quickly and peaked at approximately 50 $\mu\text{L min}^{-1}$ (black curve). As flow rates further increased, lower A1 binding with GPIB was observed. This suggests that the flow rate of 50 $\mu\text{L min}^{-1}$ established a hydrodynamic force sufficient to turn on most of the SMORES construct, inducing the release of most A1 in the flow experiment and, therefore, resulting in the highest concentration of A1 (17.55 nM) binding to GPIB in the ELISA experiment. The cumulative release of A1 as a function of flow rate is displayed as the grey curve in Fig. 5A, indicating that the binding of the released A1 to GPIB started to escalate at 50 $\mu\text{L min}^{-1}$ and complete release was achieved around 70 $\mu\text{L min}^{-1}$. This suggests a narrow range of threshold flow rates (50–70 $\mu\text{L min}^{-1}$), centered at approximately 60 $\mu\text{L min}^{-1}$, at which the shear force is sufficient to induce aptamer unfolding and subsequent release of A1 for bind with GPIB. The data point at 10 $\mu\text{L min}^{-1}$ was excluded from Fig. 5A, as free A1 from the loading step was flushed from the microfluidic device during this initial flow condition.

To correlate the flow rate response in the microfluidic experiments to the force response in the optical tweezers measurements, a COMSOL Multiphysics model was used to analyze the forces acting on the bead at different flow conditions. The force acting on the bead generated by the simulation, denoted as F_s , was subsequently used to calculate the force acting on the 45 nm-long aptamers molecules, represented as F_b through eqn (7), where θ is the angle between F_s and F_b .

$$F_b \cos \theta = F_s \quad (7)$$

This calculation was adapted from a model outlined in the Chen *et al.* paper⁶¹ (inset in Fig. 5, where R is the radius of the bead, and d is the tether length). Table S1† summarizes the simulated F_s and the corresponding F_b at different flow rates.

The cumulative A1 release profile *vs.* the flow rate from Fig. 5A was subsequently converted to the cumulative A1 release as a function of pulling force applied on the aptamer (Fig. 5B, grey curve). The flow rate window of 40–80 $\mu\text{L min}^{-1}$ for functional A1 release corresponds to a force range of 3.10–6.45 pN. To compare this force range with that predicted by the optical tweezers measurements, the unfolded percentage of the aptamer as a function of force predicted by eqn (6)

(Fig. 2F) was overlaid in Fig. 5B (black curve). A comparable trend between the grey and black curves in Fig. 5B indicates that optical tweezers measurements and flow experiments share a similar range of threshold forces to trigger a rapid shift in the aptamer conformation and payload release. The released payload is functional in binding with its receptor, the platelet GPIB receptor.

The blood flow profile is an important regulator of the balance between bleeding and clotting. Blood shear rates exhibit variability across vascular regions, encompassing physiological values of 300 to 800 s^{-1} in arteries and 15 to 200 s^{-1} in veins, while micro-arterioles demonstrate higher shear rates ranging from 450 to 1600 s^{-1} . High shear hemodynamics ($>1000 \text{ s}^{-1}$) promote elongation and activation of VWF, leading to platelet binding and clot formation.⁶² Additionally, VWF-dependent thrombus formation was observed at the outflow region of stenosis models at inflow shear rates of 600, 1000, and 2000 s^{-1} .¹⁸ Finally, the threshold of unfolding shear stress for tethered VWF is reported in the range of 20–35 dyn cm^{-2} , corresponding to shear rates up to 6000 s^{-1} in plasma.⁶³ Considering the range of reported physiological shear rates across vascular regions and threshold shear rates to activate VWF, the SMORES construct was designed to release the VWF-A1 and interact with the platelet GPIB receptor within a flow rate range of approximately 40–70 $\mu\text{L min}^{-1}$. This corresponds to a shear rate range of 2810.4–4918.1 s^{-1} in water (Table S1†), as determined by COMSOL Multiphysics simulation based on the channel dimensions. This shear rate range is comparable to the reported shear rate required to unfold VWF and initiate blood clotting.⁶²

The rational design of the SMORE construct to respond to specific flow conditions relies on the understanding of the aptamer biomechanics, which is further matched with the forces experienced in the desired shear environment. In this study, optical tweezers measurements of single aptamer molecules provided crucial biomechanical parameters to predict ARC1172's unfolded fraction as a function of force, uncovering a specific range of threshold forces that induce a rapid shift from a folded to an unfolded state. However, the aptamer molecule alone is too small to have a significant conformational change in the physiologically relevant shear rate range. For example, at a shear rate of 5000 s^{-1} , a spherical molecule 10 nm in diameter would experience a shear force on the order of atto-newtons in water at room temperature, which is insignificant relative to the pico-Newton force required to unfold the molecule, whether free-floating or immobilized on a surface. To amplify the shear force on the aptamer, the aptamer molecule is conjugated with a microparticles and immobilized to a static surface on the other end: the hydrodynamic force experienced by the particle pulls the molecule and modulates its structure and function. To match the force needed for aptamer unfolding with the force to unfold VWF, a COMSOL simulation aids in selecting the proper microparticle dimension and aptamer tether length. By combining single-molecule force measurements and simulation of hydrodynamic forces under flow, the SMORES construct releases the

biotherapeutic target under a predefined shear condition. The rational design strategy promises the translation of the SMORES strategy to other drug release applications under physiological or pathological flow patterns.

It should be noted that a buffer was used in the microfluidic flow experiments, while biofluids could have different viscosities, which can alter the shear response of the construct. To understand the construct's response in biofluids of greater viscosity, such as cell culture medium with 10% FBS and blood, we used COMSOL simulations to assess how changes in fluid viscosity affect the total force experienced by the aptamer at a given flow rate. Our results (Table S2†) demonstrated that the total force acting on the tether scales linearly with the solution viscosity. Combining Tables S1 and S2,† it is observed that the total force experienced in biofluids of greater viscosity at a certain flow rate is comparable to applying the experimental buffer at a higher flow rate. Thus, the threshold flow rate and shear rate required to unfold the aptamer and release the VWF-A1 domain payload will be lower in the higher viscosity biofluids. To mimic the shear response of VWF, the construct can be redesigned, since the threshold flow or shear rate of the construct are tunable by the bead size and tether length.

The SMORES construct offers unique advantages, providing precise tunability in releasing the payload at targeted shear rates. Additionally, SMORES can be engineered to deliver diverse payloads at specific pathological shear rates, surpassing the functionalities of naturally existing shear-sensitive biomolecules. Aptamers are used in this study as the shear responder for a few reasons. Compared to antibodies, aptamers offer the advantages of ease of systematic synthesis *in vitro*, high-purity, large-scale preparation, easy site-specific modification by chemical synthesis, high target specificity and affinity, great stability, small physical size, and better tissue penetration.^{64,65} In addition, aptamers generally exhibit low immunogenicity,⁶⁶ while their unique three-dimensional structure allows for precise target binding. Furthermore, chemical modifications can enhance their stability and further reduce immune recognition, making aptamers well-suited for systemic administration, as shown in a range of therapeutic applications.^{67,68}

Compared to shear-responsive nanomaterials based on molecular assemblies, such as shear-responsive liposomes and hydrogel particles, single-molecule-based SMORES stands out for its ability to circulate or be immobilized, achieve responsiveness down to a single effector molecule, and deliver localized functions. The modular design of SMORES holds significant potential for delivering novel functions beyond what is achievable with natural biomolecules, offering precise spatial, temporal, and on-demand responses in circulation.

4. Conclusions

In summary, this work employed a fundamental understanding about structure and function of single biomolecules under mechanical perturbation to design bioactive smart materials

with flow modulated functions. To our knowledge, this is one of the first attempts to design single-molecule-based biomaterials responsive to shear stimulation. Compared with flow sensitive materials in the literature based on molecular assemblies, single-molecule flow sensors better mimic the structure and function of circulating coagulation factors, thus are expected to have more accurate spatial and temporal control of the delivered functions. The SMORES material also shows promise in delivering bio-functions reversibly, which is difficult to achieve using conventional drug carriers. Additionally, the modular material design can be easily adapted to other sensing and drug delivery applications in regions with defined flow patterns.

Author contributions

Esraa Ismail: writing – original draft (lead); data curation (lead); validation (lead); visualization (lead); investigation & methodology (equal); formal analysis (equal); conceptualization (equal). Yi Liu: investigation & methodology (equal); formal analysis (equal); writing – review & editing (supporting). Yi Wang: investigation & methodology (equal); formal analysis (supporting); writing – review & editing (supporting). Sajedehalsadat Yazdanparast Tafti: investigation & methodology (supporting); formal analysis (supporting); validation (supporting). X. Frank Zhang: supervision (lead); funding acquisition (lead); conceptualization (lead); writing – review & editing (supporting). Xuanhong Cheng: supervision (lead); conceptualization (lead); funding acquisition (lead); writing – review & editing (equal).

Data availability

The data supporting this article have been included as part of the ESI.†

Conflicts of interest

The authors declare no conflict of interest.

Acknowledgements

The authors would like to acknowledge the generous support of the National Science Foundation (2004475). The authors would like to also acknowledge Professor Nathan Wittenberg and his team for their assistance in TIRF microscopy.

References

- 1 C. N. Trumbore, *J. Alzheimer's Dis.*, 2021, **79**, 979–1002.
- 2 C. H. H. Chan, M. Inoue, K. K. Ki, T. Murashige, J. F. Fraser, M. J. Simmonds, G. D. Tansley and N. Watanabe, *Artif. Organs*, 2020, **44**, 1286–1295.

3 T. Russo, A. Banuth, H. Nader and J. Dreyfuss, *PLoS One*, 2020, **15**, e0241040.

4 S. Pasta, V. Agnese, A. Gallo, F. Cosentino, M. Di Giuseppe, G. Gentile, G. M. Raffa, J. F. Maalouf, H. I. Michelena and D. Bellavia, *Ann. Thorac. Cardiovasc. Surg.*, 2020, **110**, 1595–1604.

5 S. Uman, A. Dhand and J. A. Burdick, *J. Appl. Polym. Sci.*, 2020, **137**, 48668.

6 M. Wei, K. Lin and L. Sun, *Mater. Des.*, 2022, **216**, 110570.

7 R. H. Ewoldt, A. E. Hosoi and G. H. McKinley, *Integr. Comp. Biol.*, 2009, **49**, 40–50.

8 S. Samimi Gharaie, S. M. H. Dabiri and M. Akbari, *Polymers*, 2018, **10**, 1317.

9 N. Zandi, E. S. Sani, E. Mostafavi, D. M. Ibrahim, B. Saleh, M. A. Shokrgozar, E. Tamjid, P. S. Weiss, A. Simchi and N. Annabi, *Biomaterials*, 2021, **267**, 120476.

10 A. Shah, M. S. Malik, G. S. Khan, E. Nosheen, F. J. Iftikhar, F. A. Khan, S. S. Shukla, M. S. Akhter, H.-B. Kraatz and T. M. Aminabhavi, *Chem. Eng. J.*, 2018, **353**, 559–583.

11 J. Pushpamalar, P. Meganathan, H. L. Tan, N. A. Dahlan, L.-T. Ooi, B. N. H. M. Neerooa, R. Z. Essa, K. Shamel and S.-Y. Teow, *Gels*, 2021, **7**, 153.

12 J. Shi, Z. Shi, Y. Dong, F. Wu and D. Liu, *ACS Appl. Bio Mater.*, 2020, **3**, 2827–2837.

13 Y. Sagara and T. Kato, *Angew. Chem.*, 2008, **120**, 5253–5256.

14 S. Yamane, Y. Sagara, T. Mutai, K. Araki and T. Kato, *J. Mater. Chem. C*, 2013, **1**, 2648–2656.

15 Y. Wang, A. V. Pisapati, X. F. Zhang and X. Cheng, *Adv. Healthcare Mater.*, 2021, **10**, 2002196.

16 S. Zeibi Shirejini, J. Carberry, K. Alt, S. D. Gregory and C. E. Hagemeyer, *Adv. Funct. Mater.*, 2023, 2303717.

17 L.-J. Chen, W.-L. Wang and J.-J. Chiu, *Mol. Cell. Mechanobiol.*, 2016, 29–56.

18 S. Okhota, I. Melnikov, Y. Avtaeva, S. Kozlov and Z. Gabbasov, *Int. J. Mol. Sci.*, 2020, **21**, 7804.

19 J. E. Sadler, *Annu. Rev. Biochem.*, 1998, **67**, 395–424.

20 H. Fu, Y. Jiang, D. Yang, F. Scheiflinger, W. P. Wong and T. A. Springer, *Nat. Commun.*, 2017, **8**, 324.

21 T. A. Springer, *Blood*, 2014, **124**, 1412–1425.

22 K. De Ceunynck, S. F. De Meyer and K. Vanhoorelbeke, *Blood*, 2013, **121**, 270–277.

23 D. Butera, F. Passam, L. Ju, K. Cook, H. Woon, C. Aponte-Santamaría, E. Gardiner, A. Davis, D. Murphy and A. Bronowska.

24 C. Aponte-Santamaría, V. Huck, S. Posch, A. K. Bronowska, S. Grässle, M. A. Brehm, T. Obser, R. Schneppenheim, P. Hinterdorfer and S. W. Schneider, *Biophys. J.*, 2015, **108**, 2312–2321.

25 C. Martin, L. Morales and M. Cruz, *J. Thromb. Haemostasis*, 2007, **5**, 1363–1370.

26 J. A. López, *Blood Coagulation Fibrinolysis*, 1994, **5**, 97–119.

27 J. Schulte Am Esch, M. A. Cruz, J. B. Siegel, J. Anrather and S. C. Robson, *Blood*, 1997, **90**, 4425–4437.

28 N. A. Arce, W. Cao, A. K. Brown, E. R. Legan, M. S. Wilson, E.-R. Xu, M. C. Berndt, J. Emsley, X. F. Zhang and R. Li, *Nat. Commun.*, 2021, **12**, 2360.

29 Y. Zhang, G. Figueroa-Miranda, C. Wu, D. Willbold, A. Offenhäusser and D. Mayer, *Nanoscale*, 2020, **12**, 16501–16513.

30 R. Li, X. Wu, J. Li, X. Lu, R. C. Zhao, J. Liu and B. Ding, *Nanoscale*, 2022, **14**, 9369–9378.

31 W.-H. Chen, S. Yang Sung, M. Fadeev, A. Cecconello, R. Nechushtai and I. Willner, *Nanoscale*, 2018, **10**, 4650–4657.

32 K. X. Tan, S. Pan, J. Jeevanandam and M. K. Danquah, *Int. J. Pharm.*, 2019, **558**, 413–425.

33 X. Chen, Y. Ma, Y. Xie and J. Pu, *Front. Bioeng. Biotechnol.*, 2022, **10**, 1002285.

34 D. Duerschmied, Y. Merhi, J. F. Tanguay, R. Hutabarat, J. Gilbert, D. D. Wagner, R. Schaub, J. L. Diener and H. A. Daniel Lagassé, *J. Thromb. Haemostasis*, 2009, **7**, 1155–1162.

35 K. Sakai, T. Someya, K. Harada, H. Yagi, T. Matsui and M. Matsumoto, *Haematologia*, 2019, **105**, 2631–2638.

36 K. Matsunaga, M. Kimoto and I. Hirao, *J. Am. Chem. Soc.*, 2017, **139**, 324–334.

37 R.-H. Huang, D. H. Fremont, J. L. Diener, R. G. Schaub and J. E. Sadler, *Structure*, 2009, **17**, 1476–1484.

38 J. Garcia, S. L. Haberichter and V. H. Flood, in *Textbook of von Willebrand Disease*, ed. A. B. Federici, E. E. Berntorp, D. Lillicrap and R. R. Montgomery, Wiley, 1st edn, 2024, pp. 73–79.

39 R.-H. Huang, D. Fremont, E. A. Tuley, J. L. Diener, R. G. Schaub and J. E. Sadler, *Blood*, 2008, **112**, 257–257.

40 X. Zhang, K. Halvorsen, C.-Z. Zhang, W. P. Wong and T. A. Springer, *Science*, 2009, **324**, 1330–1334.

41 B. Zakeri, J. O. Fierer, E. Celik, E. C. Chittock, U. Schwarz-Linek, V. T. Moy and M. Howarth, *Proc. Natl. Acad. Sci. U. S. A.*, 2012, **109**, E690–E697.

42 M. de Odrowaz Piramowicz, P. Czuba, M. Targosz, K. Burda and M. Szymoński, *Acta Biochim. Pol.*, 2006, **53**, 93–100.

43 R. Krautbauer, M. Rief and H. E. Gaub, *Nano Lett.*, 2003, **3**, 493–496.

44 C. Bustamante, S. B. Smith, J. Liphardt and D. Smith, *Curr. Opin. Struct. Biol.*, 2000, **10**, 279–285.

45 E. Evans and K. Ritchie, *Biophys. J.*, 1997, **72**, 1541–1555.

46 E. Evans, K. Halvorsen, K. Kinoshita and W. P. Wong, in *Handbook of Single-Molecule Biophysics*, ed. P. Hinterdorfer and A. Oijen, Springer US, New York, NY, 2009, pp. 571–589.

47 M. T. Woodside, W. M. Behnke-Parks, K. Larizadeh, K. Travers, D. Herschlag and S. M. Block, *Proc. Natl. Acad. Sci. U. S. A.*, 2006, **103**, 6190–6195.

48 C. Bustamante, Z. Bryant and S. B. Smith, *Nature*, 2003, **421**, 423–427.

49 Q. Chi, G. Wang and J. Jiang, *Phys. A*, 2013, **392**, 1072–1079.

50 D. Proske, M. Blank, R. Buhmann and A. Resch, *Appl. Microbiol. Biotechnol.*, 2005, **69**, 367–374.

51 S. Fontenete, N. Guimaraes, J. Wengel and N. F. Azevedo, *Crit. Rev. Biotechnol.*, 2016, **36**, 566–577.

52 R. A. Dimitrov and M. Zuker, *Biophys. J.*, 2004, **87**, 215–226.

53 C. J. Bustamante, Y. R. Chemla, S. Liu and M. D. Wang, *Nat. Rev. Methods Primers*, 2021, **1**, 25.

54 T. Strunz, K. Oroszlan, R. Schäfer and H.-J. Güntherodt, *Proc. Natl. Acad. Sci. U. S. A.*, 1999, **96**, 11277–11282.

55 Y. Li, H. Qiao, W. Yan, J. Zhang, C. Xing, H. Wang, B. Zhang and J. Tang, *J. Mol. Recognit.*, 2013, **26**, 46–50.

56 B. Basnar, R. Elnathan and I. Willner, *Anal. Chem.*, 2006, **78**, 3638–3642.

57 L. Deng, E. N. Kitova and J. S. Klassen, *J. Am. Soc. Mass Spectrom.*, 2013, **24**, 49–56.

58 M. A. Neves, O. Reinstein and P. E. Johnson, *Biochemistry*, 2010, **49**, 8478–8487.

59 A. L. Chang, M. McKeague and C. D. Smolke, *Methods in enzymology*, Elsevier, 2014, vol. 549, pp. 451–466.

60 Y. Biniuri, B. Albada and I. Willner, *J. Phys. Chem. B*, 2018, **122**, 9102–9109.

61 S. Chen, R. Alon, R. C. Fuhlbrigge and T. A. Springer, *Proc. Natl. Acad. Sci. U. S. A.*, 1997, **94**, 3172–3177.

62 S. W. Schneider, S. Nuschele, A. Wixforth, C. Gorzelanny, A. Alexander-Katz, R. R. Netz and M. F. Schneider, *Proc. Natl. Acad. Sci. U. S. A.*, 2007, **104**, 7899–7903.

63 D. Kim, C. Bresette, Z. Liu and D. N. Ku, *APL Bioeng.*, 2019, **3**, 041502.

64 S. M. Nimjee, R. R. White, R. C. Becker and B. A. Sullenger, *Annu. Rev. Pharmacol. Toxicol.*, 2017, **57**, 61–79.

65 J. Zhou and J. Rossi, *Nat. Rev. Drug Discovery*, 2017, **16**, 181–202.

66 K. D. Kovacevic, J. C. Gilbert and B. Jilma, *Adv. Drug Delivery Rev.*, 2018, **134**, 36–50.

67 J. C. Gilbert, T. DeFeo-Fraulini, R. M. Hutabarat, C. J. Horvath, P. G. Merlino, H. N. Marsh, J. M. Healy, S. BouFakhreddine, T. V. Holohan and R. G. Schaub, *Circulation*, 2007, **116**, 2678–2686.

68 T. J. Povsic, B. A. Sullenger, S. L. Zelenkofske, C. P. Rusconi and R. C. Becker, *J. Cardiovasc. Transl. Res.*, 2010, **3**, 704–716.